PCCP

ROYAL SOCIETY OF CHEMISTRY

PAPER

View Article Online
View Journal | View Issue

Cite this: *Phys. Chem. Chem. Phys.*, 2026, **28**, 3850

Structural and dynamical heterogeneities at the nanoscale in alkali/earth alkaline ionic liquid electrolytes: experiment and molecular simulation

Patrick Judeinstein, *[ab] Hoang Phuong Khanh Ngo,[c] Fabrice Cousin,[a] Cristina Iojoiu,[c] Emilie Planes[c] and Benoît Coasne *[de]

Received 8th December 2025,
Accepted 20th January 2026

DOI: 10.1039/d5cp04760a

rsc.li/pccp

Ionic liquids (ILs) are versatile solvents for a wide range of substances, including alkali and alkaline earth salts. Mixtures of ILs and these salts are promising electrolytes for Li and post-Li batteries, offering unique properties such as stability and viscosity. These characteristics stem from the multiscale coupling between structural and dynamical aspects of ILs. We focus in this study on a family of electrolytes based on the iconic IL 1-butyl-3-methylimidazolium trifluoromethylsulfonimide (BMImTFSI), in which alkali (Li^+, Na^+, K^+, Cs^+) and alkaline earth (Mg^{2+}) TFSI salts are dissolved. First, we demonstrate how classical molecular dynamics (MD) allows reproducing structural scattering features and self-diffusion coefficients, as measured by wide angle X-ray scattering and pulsed field gradient NMR. With this approach, we show that MD also helps to decipher the subtle differences between electrolytes in which alkali or earth alkaline ions are dissolved. Second, molecular dynamics analyses based on a single particle tracking strategy allows unravelling the correlations between structural and dynamical heterogeneities in a multiscale approach (from coordination spheres/fs to nanosegregation/hundreds of ns), therefore evidencing a large distribution of dynamics and the presence of clusters with long lifetime. All these results sort out time/temperature equivalence, which appears as a key to understand the behavior of nanostructured fluids.

1. Introduction

Room temperature ionic liquids (RTILs) are composed solely of ions which form a liquid at ambient temperature or even below.[1] Keeping in mind that most common inorganic salts have high melting points (*e.g.* NaCl melting point is 801 °C), this exceptional feature for a system made up of charges only results from the specific molecular architecture of RTILs. In fact, they involve an adequate combination of (i) organic cations and (ii) organic or inorganic anions, which present molecular flexibility and delocalized charges. This combination leads to a subtle balance between strong coulombic interactions and high conformational entropy.[2] Therefore, at the molecular level, these systems present antagonist features, *i.e.* ionic/polar and aliphatic/apolar moieties, which leads to a very specific nanoscale organization with strong local heterogeneities.[3–5] In addition to this specific molecular organization, the strong coulombic interactions involved in RTILs also lead to an extremely low vapor pressure, very good electrochemical and thermal stabilities, and very broad range of viscosities. Furthermore, owing to their specific chemical structures, RTILs have the unique ability to dissolve either ionic compounds or organic entities. As a result, these liquids can be tuned for a broad range of applications where they are used as specific solvents for synthesis, separation, catalysis, energy, magnetism, lubrication, heat transfer fluid.[6–9]

With these specific properties, large amount of Li salts may be dissolved in RTILs leading to electrolytes which are considered as promising candidates for advanced lithium batteries with many advantages (thermal stability, sustainability, low cost and efficiency, safety aspects).[10] In particular, they can be used in both standard and extreme conditions (low or high pressure/large range of temperature).[11,12] However, the growing need for specific systems dedicated to various applications in this field also requires the development of specific and/or post-lithium batteries based on other metal redox couples such as sodium, potassium, magnesium, calcium, aluminum or zinc ions.[13] In this context, the opportunity to use IL-based electrolytes for such new generation of devices has already been

[a] *Université Paris-Saclay, CEA, CNRS, LLB, 91191, Gif-sur-Yvette, France. E-mail: patrick.judeinstein@cnrs.fr*
[b] *Université Paris-Saclay, CNRS, Laboratoire de Physique des Solides, 91405, Orsay, France*
[c] *Univ. Grenoble Alpes, Univ. Savoie Mont Blanc, CNRS, Grenoble INP, LEPMI, 38000 Grenoble, France*
[d] *Univ. Grenoble Alpes, LIPhy, F-38000 Grenoble, France. E-mail: benoit.coasne@univ-grenoble-alpes.fr*
[e] *Institut Laue Langevin, F-38042 Grenoble, France*

fostered to R&D stages with promising results.[13–15] More broadly, the propensity of ionic liquids to dissolve more or less selectively metal salts has also applications in various other fields such as purification or extraction technologies.[16] Nonetheless, subtle differences of salt solubility inside an homologous series (same anion, various cations) may be rationalized in terms of size, surface charge density, polarizability, electronegativity, HOMO/LUMO energies (*i.e.* hard/soft scale) of the different alkali/alkaline earth cations.[17,18] However, systematic fundamental studies based on experimental, molecular simulation or theoretical approaches remain scarce.[19–22]

We recently investigated experimentally the properties of a series of alkali/alkali earth electrolytes based on the mixture of 1-butyl-3-methyl-imidazolium bis(trifluoromethylsulfonyl) imide (BMImTFSI) with alkali (lithium, sodium, potassium, cesium) and earth alkali (magnesium) TFSI salts (XTFSI, X = Li, Na, K, Cs, Mg) at various concentrations.[23] The transport properties of these electrolytes were analyzed over a wide range of temperatures using a multi-technique approach: viscosity, conductivity and diffusivity. Correlations between viscosity and ionic conductivity measurements as determined using a Walden plot indicate that all these electrolytes are ''good ionic conductors'' according to Angell's classification.[23] Furthermore, these experiments provide evidence that transport properties measured at room temperature are strongly affected by the nature and the concentration of the added alkali/earth alkali added ions. However, when these measurements are performed over a broad range of temperatures including conditions near to the electrolyte glass transition temperature T_g, a master curve is obtained as the corresponding data collapse onto a single plot for all alkali cations and concentrations. Nonetheless, despite this general behavior, subtle yet noticeable differences are observed between monovalent alkali and divalent earth alkali ions. While these differences point to specific individual and collective transport behaviors, their underlying molecular mechanisms remain to be identified. In this framework, joint experimental and classical molecular dynamics approaches appear as a powerful strategy to describe finely these systems.[24–26] In more detail, the synergy between these two approaches allows one to decipher the structure and dynamics of RTIL-based electrolytes at the nanoscale. In particular, when a reasonable forcefield and methodology are employed, molecular dynamics (MD) simulations not only reproduce experimental results with precision but also provide deeper insights. For instance, MD enables the characterization of ion-correlation modes and lifetime of ion pairs, which are not otherwise difficult to measure experimentally.[25]

In this paper, we employed a combined experimental and molecular simulation strategy to delve the properties of BMImTFSI/XTFSI electrolytes. In more detail, we investigate the role of (i) the nature of the cation (X = Li, Na, K, Cs, Mg), (ii) the ionic concentration, and (iii) the temperature. First, the comparison of molecular simulation results with experimental data for both structural and dynamical features (X-ray scattering and NMR self-diffusion coefficients) allows us to assess the quality of the employed MD forcefield and methodology. Second, MD allows us to decipher the molecular structure of these complex electrolytes (*e.g.* cation coordination shell and aggregation) as well as to elucidate transport processes on a large time range and ion-pairing lifetime. Third, through in-depth analysis of MD trajectories, we reveal pronounced heterogeneities in the dynamical properties when the ions present in the mixtures vary. We relate such dynamical heterogeneities to very different local coordination sheathes but also to different physical chemistries when considering alkali and earth-alkali based electrolytes.

2. Methods

2.1. Experimental methods

2.1.1. Sample preparation. 1-Butyl-3-methylimidazolium bis(trifluoromethylsulfonyl)imide (BMImTFSI) and cesium bis (trifluoromethylsulfonyl)imide (CsTFSI) were purchased from Solvionic, lithium bis (trifluoromethyl sulfonyl) imide (LiTFSI) from Aldrich and used as received. Sodium, potassium and magnesium bis(trifluoromethylsulfonyl)imides (NaTFSI, KTFSI, $Mg(TFSI)_2$ respectively) were synthesized from an acid–base reaction and purified following the procedure described in our previous work.[23] The purities of the different starting chemicals (commercial and synthesized) are better than 98% and the amount of water below 100 ppm as measured by Karl Fisher method. Such low amount is not easily detected by ^{1}H NMR. The electrolytes considered in this study were prepared by mixing the required amount of BMImTFSI and alkali–TFSI salt in an argon filled glove box. The mixtures were stirred at 80 °C until homogeneous solutions are obtained and then cooled to RT to confirm the complete dissolution of the salt. Solubility was deemed sufficient if the solution remains clear without cloudiness or solid particles after standing for 72 h at RT. In this work, the electrolytes are named [X][BMIm][TFSI]f where X represents the alkali/earth alkaline cation and f is the molar fraction of dissolved salt, defined as the number of M^{n+} ions per the number of $BMIm^+$ cations (f = M/BMIm). The f was varied between 0.1 and 0.4.

2.1.2. X-ray scattering. Wide angle X-ray scattering (WAXS) measurements were performed on a laboratory XEUSS 2.0 instrument (Xenocs, France). The instrument uses a microfocused Cu K_α source with a wavelength of 1.54 Å (corresponding to a beam energy of 8 keV) and a 2D Pilatus3 detector (Dectris, Switzerland). The sample to detector distance was set to 0.168 m to yield an accessible Q range of 0.08 $Å^{-1}$–2.9 $Å^{-1}$ compatible with the MD analysis. In this geometry, the whole instrument, including sample holder is under vacuum. The experiments were performed with a collimated beam size of 0.5×0.5 mm^2. The sample distance of the setup was calibrated before each set of measurements in using the diffraction peaks of a reference silver behenate sample. The liquid samples were introduced into X-ray glass capillaries of 1.5 mm diameter (WJM-Glas, Müller GmbH, Germany) in a glove box and sealed, and 1.5 hours acquisition was required. However, electrolyte containing cesium ions absorb strongly X-rays and it requires to use 0.2 mm thick borosilicate flat capillaries from Vitrocom®

as the best compromise between absorption (glass walls plus IL sample) and scattered signal. Angular averaging was performed and scattering from empty beam, capillaries and dark field were measured independently and subtracted using standard protocols.

2.1.3. Pulsed field gradient nuclear magnetic resonance. Self-diffusion coefficients were measured by pulsed-field gradient nuclear magnetic resonance (PFG-NMR) using a Bruker 400 Avance III HD spectrometer (frequencies are 400.13, 376.50 and 155.51 MHz for ^{1}H, ^{19}F and ^{7}Li, respectively) and a Bruker 300 Avance III spectrometers for ^{133}Cs PFG-NMR (frequency: 39.35 MHz), both equipped with 5 mm diffusion probe and temperature regulation unit (20–80 °C, accuracy and stability ±2 °C). ILs were filled into small diameter tube (d = 4 mm) in the glove box, then were flame sealed to prevent the humidity. Stimulated echo sequence was used. The maximum magnitude of the pulsed field gradient for both spectrometer was 900 G cm^{-1}, the diffusion delay Δ was adjusted between 50 ms and 100 ms, and the gradient pulse length δ was set between 1 ms and 5 ms depending on the diffusion coefficient and the nature of the mobile species. At higher temperature, some measurements were also performed with Δ = 200 ms to confirm that no convection artifacts occur. The self-diffusion coefficients were determined from the classical Stejskal–Tanner equation:[27]

$$\ln(I/I_0) = -D(G\gamma\delta)^2(\Delta - \delta/3) \quad (1)$$

where G is the magnitude of the two gradient pulses applied, γ is the gyromagnetic ratio of the nucleus under study and I and I_0 are the integrated intensities of the signal obtained respectively with and without gradient pulses. Here, we used 16 equally spaced gradient steps for each experiment and the number of scans was adjusted to obtain good signal to noise ratio. Repetition rate between scan was set to 5 T_1 (typically 10 to 15 s) to allow a complete relaxation of the spins and the acquisition of quantitative data. For such experiments, frequency lock is not necessary as the magnetic field is stable enough even for long acquisition and homogenity of the magnetic field is performed by optimization of the NMR FID signal. Data acquisition and treatment were performed with Bruker Topspin software.

2.2. Computational methods

The structure and dynamics of the BMImTFSI/XTFSI electrolytes were simulated by means of classical molecular dynamics (MD) using an all-atom description. All molecular simulations were performed using LAMMPS package (version 2Jul2021).[28] The imidazolium-based IL was described using the classical force field developed by Canongia Lopes *et al.*[29] with its new parameterization by Köddermann *et al.*[30] Parameters determined by Netz and coworkers were used for the alkali[31] and earth alkali[32] cations. In all of these force fields, the overall cation and anion charge is unity ($q = \pm 1e$) with each atom X in the ion carrying a partial charge ($|q_X| \leq 1e$).

Interactions between the different atoms were calculated as the sum of the dispersion interaction with a repulsive short-range contribution and the Coulombic interaction. The repulsion–dispersion interactions were described using a Lennard-Jones potential, in which the cross-parameters σ_{kj} and ε_{kj} between atom types k and j are obtained from the Lorentz–Berthelot mixing rules of like-atom pairs. The like-atom parameters for the IL were taken from ref. 33. The electrostatic interactions were calculated using the Ewald sum technique to correct for the finite size of the simulation box (the parameters were chosen so that the relative accuracy is 10^{-5}). More details are provided in the SI (Fig. S1 and Table S1).

Simulation boxes containing 124 ion pairs (box size $L \sim 35$ Å with compositions given in Table S2) were used to determine quantities related to dynamical parameters (self-diffusion coefficients, ion-paring and association mode lifetimes) (Fig. 1). Even if the size of these simulation boxes are rather small compared to other studies (which may induce some systematic variations of diffusion coefficients,[34] this choice was guided by the need to maintain a reasonable computation time – given the number of systems under study and the duration of the trajectories required for our analysis. In addition, significantly larger systems, obtained by using 3 × 3 × 3 duplicated simulation boxes and containing 3348 ion pairs (box size $L \sim 100$ Å) were also considered for the structural studies. These larger systems enable the investigation of characteristic sizes exceeding the observed heterogeneities. In particular, such large system sizes allow probing length scales compatible with the scattering vector range measured in WAXS experiments (0.1 Å^{-1} < Q < 3.2 Å^{-1} corresponding approximately to distances in the range of 2 Å < l < 60 Å). The temperature T and pressure P were controlled using a Nosé–Hoover thermostat and barostat (relaxation time constants of 0.01 and 0.1 ps, respectively).[35] The molecular dynamics simulations were integrated using the Verlet algorithm with a timestep of 1 fs. For all trajectory calculations, and another 1 ns equilibration run was first performed in the NPT ensemble (P = 1 bar, T = 500 K) to bring the system to equilibrium, and then the system was quenched at the studied temperature, and another 1 ns equilibration run was performed (NPT ensemble, P = 1 bar, T desired) to ensure the stabilization of the total energy of the system and of the size of the simulation cell (Fig. S2). Then, another NVT equilibration run (~1 ns) was performed before acquiring data in a final production run. Some short dynamical trajectories were used to obtain very accurate mean-square displacements at short times: 0.1 ns trajectories were recorded with a 10 fs sampling timestep. For longer dynamics, up to 200 ns trajectories with a 1 ps sampling timestep were used.

For the larger boxes used for the structural study, 50 configurations were used in the NPT ensemble and a large sampling timestep of 1 ps was considered to ensure that the different configurations are statistically uncorrelated.

3. Results

Results obtained from molecular dynamics studies are relying on an adequate choice of forcefield and methodologies and its validation requires to compare how simulation results compare with real-world experiments. The aim of this section is to

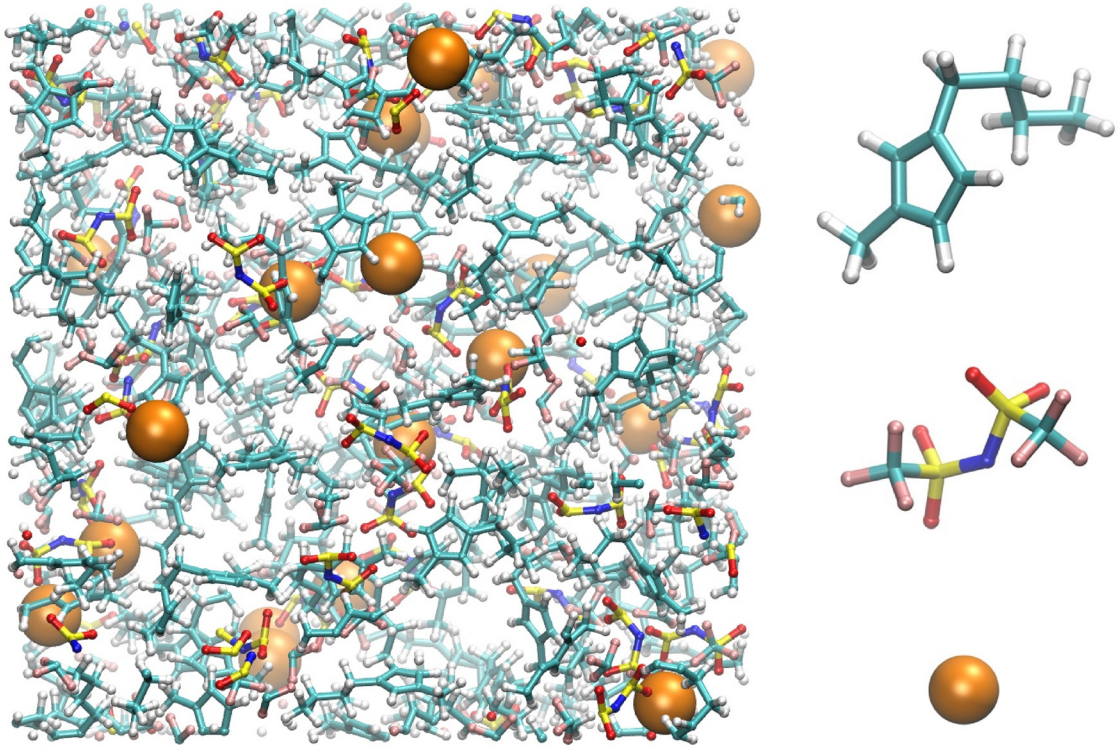

Fig. 1 Typical molecular configuration used to study properties for ionic liquid based electrolytes by molecular dynamics. This sample contains 104 $BMIm^+$ cations, 20 Li^+ and 124 $TFSI^-$ anions, corresponding to [BMIm][Li][TFSI]*0.2* composition. The box is at T = 300 K and its size is $L \sim 38$ Å in each direction. Each ion type is presented on the right, BMIm (top), TFSI (middle), Li^+ (down). Colored atom representation is carbon: cyan, hydrogen: white, fluorine: pink, sulfur: yellow, oxygen: red and nitrogen: blue and Li^+: orange.

compare results obtained through these two approaches – either for structural (*e.g.* coherent structure factor $S(Q)$) or dynamical (*e.g.* individual self-diffusion coefficients D_i) aspects.

3.1. Structure

Fig. 2a presents the experimental X-ray scattering data for pure BMImTFSI and BMImTFSI/XTFSI electrolytes for the higher salt concentrations (X = Li^+, Cs^+, f = 0.4 Mg^{2+} f = 0.2) in the range 0.1 $Å^{-1} < Q < 2.5$ $Å^{-1}$ at room temperature. For ionic liquids, this scattering vector range allows us to probe the nanostructuration of these complex liquids, resulting from a competition between entropic disordering forces and coulomb ordering. Fig. 2b presents the total scattering function $S(Q)$ for the same electrolytes as calculated from molecular dynamics trajectories.

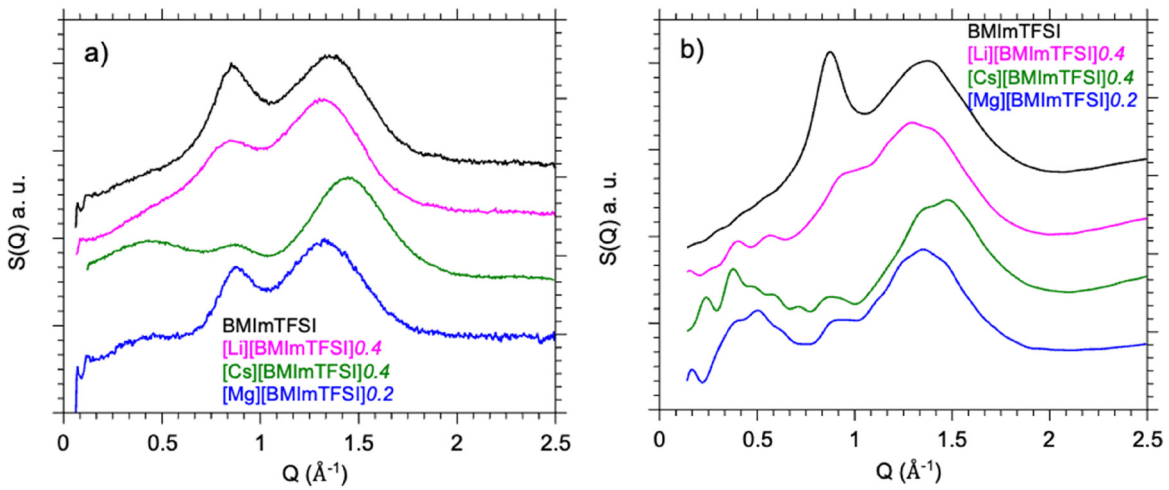

Fig. 2 WAXS diffraction pattern of pure BMImTFSI and [X][BMImTFSI]f electrolytes (X = Li^+, Cs^+, f = 0.4 Mg^{2+} f = 0.2) (a) experiments at room temperature (b) molecular dynamics at T = 300 K. These patterns are shifted vertically for the sake of clarity.

Results corresponding to intermediate composition are also presented in supplementary information (Fig. S3). For all mixtures, a strong agreement is observed between the molecular simulation approach and the experimental data, which already indicates that our MD strategy is reasonably robust to get structural information on our mixtures.

Pure BMImTFSI presents two strong peaks, a broader one around Q = 1.36 Å^{-1} and a narrower at Q = 0.85 Å^{-1}. The first one is observed in all ionic liquids and is assigned to inter and intramolecular contributions related to the neighboring species (*i.e.* anion pair atoms, adjacent tails, cation–anion neighbors). The second one is only observed for ionic liquids with larger anions and is then attributed to correlations between anions, and between the head group of imidazolium ring and the anion.[3] Its shape is strongly modified when adding alkali or earth alkaline cations to the mixture. Moreover, a third component at lower Q appears as a shoulder around 0.5 Å^{-1} for Li^+ or a peak around 0.4 Å^{-1} for Cs^+ and Mg^{2+} (Fig. S3). Such correlation at lower scattering vector (*i.e.* it corresponds to longer correlation distances) reflects some structural inhomogeneity at the nanometer scale.[35] Such peak in the low-Q domain is also sometimes referred to as a prepeak (or first sharp diffraction peak) and found in ionic liquids when a long alkyl chain is linked to the ionic core (ammonium, imidazolium) but also in some other ionic liquids when lithium salt is added.[25,37,38] This correlation reflects a self-organization inside the liquid at a real space distance ($d \sim 2\pi/Q$) in the 1–2 nm range which is comparable to the molecular size of the imidazolium cation (0.7–1 nm depending on its configuration). As the intensity of this peak increases strongly with the addition of more Cs^+ and Mg^{2+} cations, it shows that the repetition structure occurs over few domains. It points out that these liquids get some nanoscale structuration corresponding to the segregation between polar/ionic counterpart and apolar moieties – as already discussed in the literature.[13,38,39] In the meantime, with the addition of alkali salt, the amplitude of the medium peak is decreasing while the peak at larger scattering vector shifts to lower value (longer correlation distances) with addition of Li^+. These effects are evolving slightly with the nature of the cation (*cf.* Fig. S4 for Na^+ and K^+ cations) up to inversion and are even more pronounced when Cs^+ is added. Comparable trends have been also observed in other ionic liquids based electrolytes based upon doping with various alkali cations.[40]

3.2. Dynamics

The self-diffusion coefficients D_i of the different species i inside these mixtures – imidazolium cation ($BMIm^+$), trifuorosulfonimide ($TFSI^-$) and Li^+ and Cs^+ alkali cations – were measured experimentally by means of ^{1}H, ^{19}F, ^{7}Li and ^{133}Cs PFG-NMR respectively.[23] In parallel, molecular dynamic simulations were performed to obtain mean square displacements of the center of mass of the different species and to infer self-diffusion coefficients. These results, presented in Fig. 3 (with complementary results provided in Supplementary data, Fig. S5 and S6), show good agreement between PFG-NMR experiments and MD. Notably the MD values are consistently slightly higher than experimental values.

Fig. 3 presents the evolution of self-diffusivities D_i of the different species i inside [X][BMImTFSI]*0.2* electrolytes at T = 298 K as obtained from PFG-NMR experiments and analyses of MD trajectories. For pure BMImTFSI (f = 0), diffusion coefficient for BMIm is slightly higher than for TFSI as it was already measured and computed in previous work.[36,41,42] This difference is related to the relative mass of both ions and high dissociation ratio, corresponding to rather uncorrelated long range translation motion. Lower values are measured by NMR as it was also sketched in previous work. However, further NMR experiments

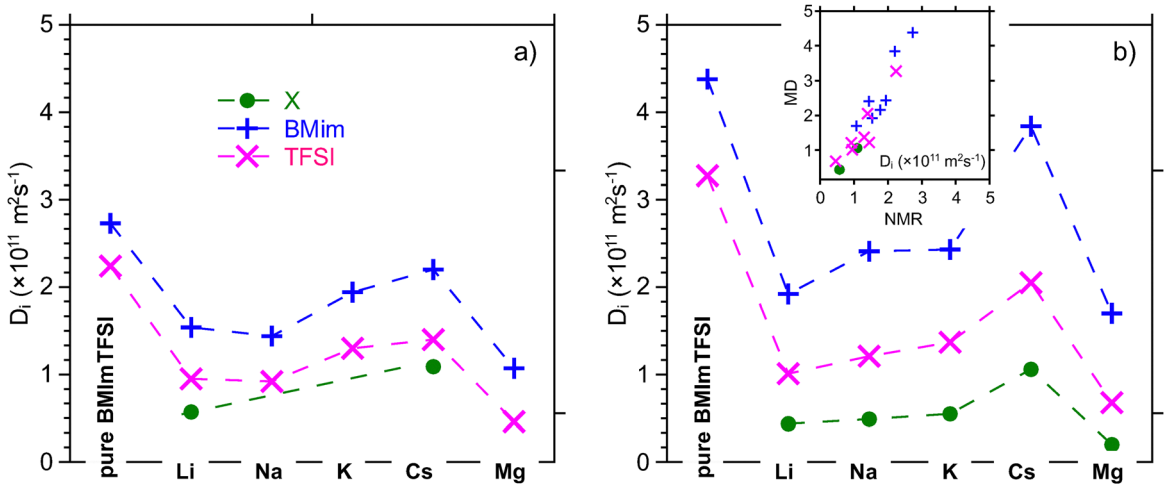

Fig. 3 Comparison of self-diffusion coefficients D_i as determined from (a) PFG-NMR experimental measurements[23] and (b) MD mean square displacements for [X][BMImTFSI]*0.2* (X = Li^+, Na^+, K^+, Cs^+, Mg^{2+}. (298 K for NMR, T = 300 K for MD). Direct comparison between experimental and MD values, which are presented in the inset, show good agreement between the values. Uncertainities, which are not displayed on the graph for the sake of clarity, are around 10% for both NMR experimental and MD values.

and MD simulations were also performed for this system on a larger temperature range (up to T = 350 K and T = 500 K for NMR and MD respectively). The corresponding results, which are presented in Fig. S5a, also show strong agreement between these two approaches on this large temperature range.

The impact of the addition of alkali/earth alkali ions is also presented in Fig. 3 as well as in Fig. S5 and S6. It yields to a significant decrease of mobility for both BMIm and TFSI species as the self-diffusion coefficient of alkali cation is remarkably smaller (as measured for Li^+ and Cs^+ and computed for all ions). This effect has already previously been reported in a wide range of ionic liquid based electrolytes. In fact, even if the alkali is the smallest/lightest species of the mixtures, a strong complexation by the anion leads to a larger effective species (*i.e.* less mobile).[37,43–45] These association effects are also noticeable for the TFSI anions. Such cation–anion associations were already depicted in some similar systems from Infrared, Raman and NMR spectroscopies,[46,47] and supported by MD analysis in various similar systems. It was also further analyzed in these electrolytes on the basis of molecular dynamics.[20,48] At constant molar ratio, this effect is more pronounced for the smallest Li^+ cation than the larger Cs^+. These effects are also evidenced from the MD approach allowing to get a more complete overview on these systems. Experimental and MD results are presented in Fig. 3b. It highlights that the hindrance of BMIm and TFSI translational mobility is more pronounced for Li^+ and Mg^{2+} and decreases slightly as the alkali ion becomes bigger. This effect is consistent with those observed in dilute aqueous electrolyte, where bigger anions correspond to lower charge surface densities, less interactions with solvent/water molecules and a decrease of the size of the effective hydrodynamic radius.[49]

Here, in IL, composed of ions, the size of the mobile species is determined by the average size/molecular weight of the alkali cation and its average complexation sheath, as well as the stability and lifetime of bigger clusters (based on more than one alkali cation) as it will be detailed later. The validity of our molecular modelling approach is also confirmed from the comparison of self-diffusion coefficients, as obtained from NMR experiments and MD trajectories analysis on a large range of temperature as presented in Fig. S5b and c. They evidence a free-volume like dependence as it was also measured from viscosity and ionic conductivity measurements.[47]

4. Discussion

4.1. Structure

The total scattering structure factor is a weighted sum of all partial structure factors $S_{ij}(Q)$ between each pair of atoms i,j (eqn (2)):[50]

$$S(Q) - 1 = \left(\sum_{i=1}^{n} c_i b_i\right)^{-2} \sum_{i,j}^{2} (c_i, c_j)^{1/2} b_i b_j \left[S_{ij}^{\mathrm{AL}}(Q) - \delta_{ij}\right] \quad (2)$$

where $c_i = N_i/N$ is the mole fraction of atom type i, b_i the scattering length of atom type i (which is proportional to the number of electrons in the atom for X-ray scattering) and $S_{ij}^{\mathrm{AL}}(Q)$ are the partial structure factor between each atom pair i and j. They are derived within the Ashcroft-Langreth formalism[51] from the partial radial distribution function, $G_{ij}(r)$, which are themselves calculated from the MD trajectories:

$$S_{ij}^{\mathrm{AL}}(Q) - \delta_{ij} = 4\pi\rho(c_i c_j)^{1/2} \int_0^\infty r^2 \left[G_{ij}(r) - 1\right] \frac{\sin Qr}{Qr} \mathrm{d}r \quad (3)$$

where δ_{ij} is the Kronecker delta function. Different aspects of the structure of liquid organization in ionic based electrolytes can be highlighted more efficiently either from the partial radial distribution functions $G_{ij}(r)$ or the partial structure factor $S_{ij}(Q)$. These calculations make it possible to analyze liquid organization from an atomic site-to-site perspective. They also allow us to gather a series of partial structure factor $S_{\mathrm{AB}}(Q)$ to highlight the contributions and interactions of specific chemical groups or species (i, j denotes atoms while A and B represents center of mass (COM) of ions). Fig. 4 presents the total structure factor $S(Q)$ and the partial contributions $S_{\mathrm{AB}}(Q)$, based on the COM of the different ions as well as the corresponding partial radial pair distribution $G_{\mathrm{AB}}(R)$ for pure BMImTFSI and the more concentrated electrolytes based on Cs^+ (f = 0.4, Fig. 4b) and Mg^{2+} (f = 0.2, Fig. 4c); these electrolytes being chosen at the highest concentration of salt that enhance all effects, which are gradual with concentration as presented in supplementary information (experimental and corresponding calculated $S(Q)$ on Fig. S3 and S4 and corresponding radial distribution functions $G_{\mathrm{AB}}(R)$ on Fig. S7). The structure factor $S(Q)$ of BMImTFSI presents a broad peak centered at $Q \sim 1.4$ Å^{-1} and a small and narrower peak around $Q \sim 0.8$ Å^{-1}. Assignments of these two contributions are highlighted from the decomposition of the total structure factor $S(Q)$ into the partial structure factor $S_{\mathrm{AB}}(Q)$ of the COM description. The narrower peak at lower Q corresponds to the positive cation/cation and anion/anion contribution, which are counterbalanced by a negative anti-peak corresponding to cation/anion correlations. These partial signals are rather intense and narrow and they partially compensate each other when they are summed, as was also observed for other ILs.[52] This provides evidence for a well ordered sequence of alternating cations and anions as a signature of a well-organized liquid and tagged as the charge signature. In BMImTFSI, the second scattering peak is observed around Q = 1.5 Å^{-1} and also corresponds to cation/anion, anion–anion and cation–cation correlations. This peak, which corresponds to most diffuse interactions between molecular segments, is found in all ionic liquids and corresponds to adjacency arising from intra or intermolecular correlations.[52]

Upon addition of alkali or earth alkaline cations, strong modifications of the structure factor $S(Q)$ are observed: (i) the decrease of intensity of the peak around $Q \sim 0.8$ Å^{-1} and (ii) the appearance of a wide peak at smaller scattering vector around $Q \sim$ 0.3–0.4 Å^{-1}. These effects are getting more pronounced upon increasing the concentration and the molecular mass of the added cation as can be observed from experiment and MD approach (Fig. S3 and S4). Origins of these transformations are clearly evidenced from the COM partial

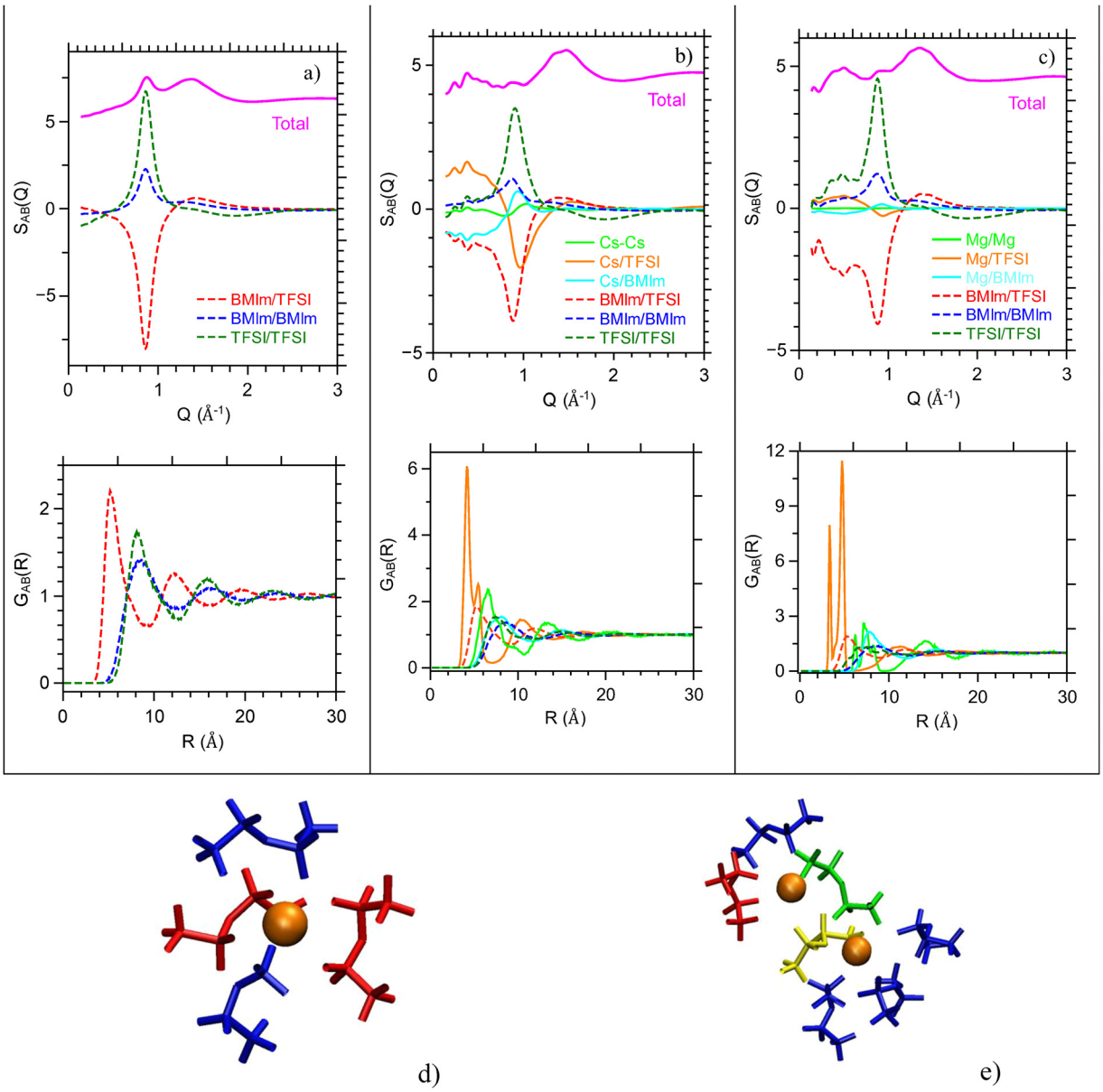

Fig. 4 Description of the structure of [X][BMImTFSI]*f* electrolytes at T = 300 K: total and partial structure factors (top) and corresponding partial radial pair distributions (bottom) in a COM description for (a) f = 0 (neat BMImTFSI) (b) [X] = Cs, f = 0.4 (c) [X] = Mg, f = 0.2. Molecular representation of (d) an isolated Cs monomer $(CsTFSI_4)^{4-}$ and (e) a Cs dimer $(Cs_2TFSI_7)^{5-}$. TFSI are in different configurations: (blue) monodentate with one Cs, (red) bidentate with one Cs, (green) TFSI bridging two Cs^+, monodentate on both sides, (yellow) TFSI bridging two Cs^+, bidentate on one side, monodentate on the other side.

structure factor $S_{AB}(Q)$ analysis (Fig. 4a–c); even if the appearance of $S(Q)$ are rather similar for [Cs][BMImTFSI]*0.4* and [Mg][BMImTFSI]*0.2*, they correspond to two different changes of the partial scattering scheme. In the case of Cs^+, its high electronic number is related to a strong scattering length and the structural correlations related to cesium are getting strong. Most specifically, the Cs-TFSI correlations lead to a strong and broad peak at low Q and a narrow and strong antipeak around $Q \sim 1$ Å^{-1}, while simultaneously the correlations corresponding to the raw BMImTFSI ionic liquid are broadening and decreasing. A small Cs–Cs contribution also appears. It indicates that introduction of Cs^+ disrupt the structural organization within the ionic liquid as Cs^+ coordinates with $TFSI^-$ anions clusters, leading to the formation of Cs centered aggregates (as will be detailed in the next section). In the case of the addition of Mg^{2+}, modification of $S(Q)$ arises from a strong modification of the initial correlations of the raw ionic liquid with also the appearance of a strong contribution below 0.6 Å^{-1} for both TFSI/TFSI and BMIm/TFSI (also BMIm/BMIm not presented here). Moreover, the addition of Mg^{2+} leads to a strong reorganization of the ionic liquid with an efficient nanostructuration at the nanometer scale.

More details about the change of local coordination sheath are deciphered from the COM radial distribution functions $G_{AB}(r)$ which are presented also in Fig. 4a–c for BMImTFSI, [Cs][BMImTFSI]*0.4* and [Mg][BMImTFSI]*0.2* (see also Fig. S7 for other [X][BMImTFSI]*f* compositions). The large number of oscillations in the partial distribution functions provide evidence for the strong degree of organization between cations and anions, which extends up to more than 3 nm (4 layers) in pure BMImTFSI. This organization is strongly affected when alkali cations replace the $BMim^+$ but still remains beyond more than one coordination layer. However, major changes are observed in the coordination of $TFSI^-$ anions, which present a strong correlation with the added alkali/earth alkaline cations. The ordering of this coordination shell is evidenced by the amplitude of the correlation peaks which splits into two components corresponding to two coordination modes of the TFSI anion around a cation: the bidentate corresponding to shorter distances and monodentate corresponding to longer distances (*cf.* molecular scheme in Fig. 4d).

Other geometries arise when alkali cations are forming some aggregates (Fig. 4e) and TFSI are bridging the Cs^+ cations. Similar distances are then measured between Cs^+ and $TFSI^-$ COM. All these configurations coexist for all alkali cations, but the ratio of the two configurations differs slightly with the nature of the cation and also the concentration of the added salt (Fig. S7). The pair distribution function $G_{X-X}(r)$ corresponding to the distance between two alkali cations also presents well-defined oscillations, which indicate the presence of dimers or even larger salt aggregates as will be discussed in the following sections.

We note that addition of Mg^{2+} leads to stronger and sharper correlations with their close shells, therefore indicating more structured coordination shells. The number of TFSI and nearest X ions in the coordination shell of the alkali cation are obtained from the numerical integration of the $G_{X-TFSI}(r)$ and $G_{X-X}(r)$ functions respectively as presented in Fig. S7 and Table 1. These findings are in agreement with those depicted from spectroscopic studies.[53] The number of anions in the coordination sphere is around 4 for alkali ions with a slight dependence with the nature of alkali and increases with salt concentration. On the other hand, it is around 5–6 for Mg^{2+} electrolytes and decreases with the concentration. Even at low alkali concentrations, a noticeable amount of alkali ions is present in the second coordination shell. It increases slightly with the atomic number of the cation and more noticeably with the amount of salt – reaching up to 3 for larger concentrations. Also, this proximity is much less in the case of the divalent Mg^{2+}. These differences are also sketched from the ratio of cations which are associated through TFSI anions. In the case of alkali ions, a single anion may link to two cations but is also sometimes engaged in the complexation, while two TFSI anions are engaged to link to two Mg^{2+} ions. Analysis of the size distribution of the clusters shows that they reach larger average sizes upon increasing the ratio of alkali ions (typically a large number of clusters with 3, 5 and 8 alkali are observed for f = 0.1, 02 and 0.4 but few larger clusters are also observed) and smaller for earth alkaline (only dimers are observed for f = 0.1, larger clusters for f = 0.2).

4.2. Dynamics

Fig. 5 presents the mean square displacements (MSD) for the center of mass of the different components ($\Delta r_i^2(t) = \langle (r_i(t) - r_i(0)) \rangle^2$ where the brackets denote statistical average over representative configurations of the system in the NVT ensemble). We show the data for the pure BMImTFSI, [Li]*0.2* and [Mg]*0.1* electrolytes computed at T = 300 K and T = 500 K. These trajectories present various motional regimes corresponding to different characteristic time scales.[54]

(1) At shorter times (lower than 1 ps), ballistic regime of COM is evidenced as MSD $\sim t^2$ for both $BMIm^+$ and $TFSI^-$. This regime corresponds to the very local translations of species before interacting with their neighbors. This time domain covers amplitude motion below 1 Å and corresponds to Debye Waller and vibrational modes as already discussed for similar systems.[54] However, smaller alkali/earth alkali cations present a more complex behavior (non monotonous) which is identified as wobbling and rattling modes inside complexation cavities.[37,55,56] These modes are more clearly evidenced from the short time velocity autocorrelation function (vacf) plots (inset of Fig. 5b). They show multiple oscillations regimes with an apparent period depending on the nature of the alkali/earth alkali cations. Their characteristic frequencies may be retrieved from a Fourier transform analysis (Fig. 5b). Each of them presents many transitions, which may be related to alkali ion in some specific location or different motion modes, and a strong shift is observed between the different alkali corresponding to the difference of mass m.[57]

(2) At intermediate times (1 ps–10 ns), a non-Gaussian regime is observed as MSD $\sim t^{\alpha}$ with $0.5 < \alpha < 2$. This regime corresponds to displacements in the order of 0.1–1 nm. In fact, this regime corresponds to a combination of molecular localized motions such as rotation, tumbling, chain conformation changes and short range displacements which are difficult to decorrelate.

Table 1 X^+ coordination and molecular environment in ionic liquid electrolytes based on XTFSI/BMImTFSI as a function of the nature of the cation and the concentration at T = 300 K. The values were determined by integrating the corresponding $G_{ij}(r)$ (*cf.* Fig. S7 in SI)

T (K)	X cation	Li^+			Na^+	K^+	Cs^+			Mg^{2+}	
	f	0.1	0.2	0.4	0.2	0.2	0.1	0.2	0.4	0.1	0.2
300 K	Number of $TFSI^-$ in X coordination shell	3.8	3.9	3.8	4.1	4.2	4.2	4.3	4.6	5.8	5.2
	Number of X^+ in X coordination shell	0.5	1.2	2.5	1.2	1.4	0.7	1.8	3.2	0.4	0.9
	% X^+ monomer	81	59	40	58	56	71	46	28	80	70

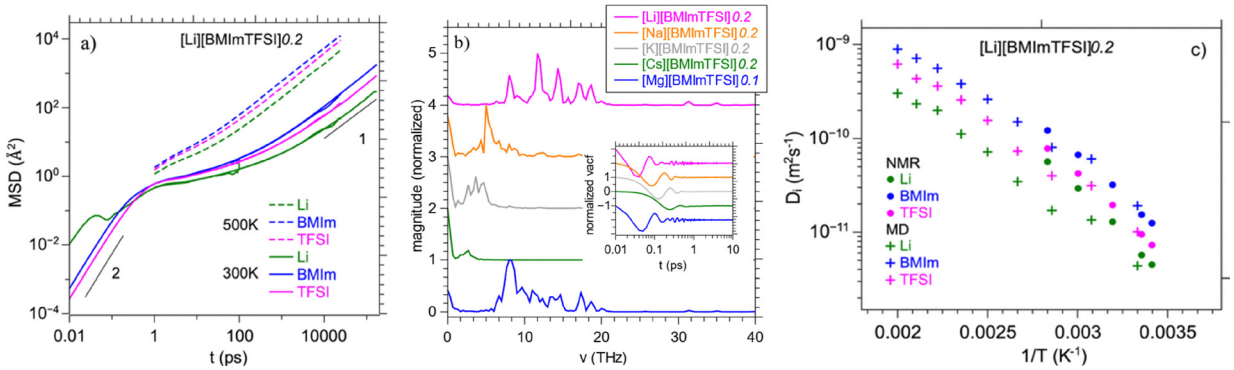

Fig. 5 Dynamic properties of [X][BMImTFSI]*f* electrolytes. (a) Mean square displacements Δr^2 as a function of time t for [Li] f = 0.2 at T = 300 K and T = 500 K. The green, blue and magenta lines correspond to the results for the center of mass (COM) for the X alkali cation, BMIm cation and TFSI anion, respectively. In each panel, the black solid lines indicate the ballistic regime $\Delta r^2 \sim t^2$ as encountered at short times and the Fickian regime $\Delta r^2 \sim t$ corresponding to self-diffusion at longer times. Short and long trajectories (see computational methods section) are merged to probe dynamics on a large time scale [0.01 ps–175 ns]. (b) Phonon spectra/magnitude spectrum for the different alkali in these electrolytes obtained by Fourier Transform of vacf (presented in the inset) to obtain rattling frequencies of the cations inside these electrolytes (10 THz = 333 cm^{-1}). (c) Evolution of individual self-diffusion coefficients with temperature. Comparison of NMR experimental values with MD for [Li][BMImTFSI]*0.2*. Similar plots for BMImTFSI and [Cs][BMImTFSI]*0.2* are presented in Fig. S5.

(3) At long times (typically above 10 ns), Fickian regime is attained as MSD $\sim t$ for the different ions of the electrolytes. The characteristic time to reach this regime is larger at lower temperatures as expected. This regime corresponds to the long range translational motion regime with displacements at the nanometer scale and above – *i.e.* much larger than the size of the species. Individual self-diffusion coefficients D_i of the different species can then be extracted using Einstein formula $\Delta r_i^2(t) = 6D_i(t)$. These values can be compared with those obtained by pulsed field gradient NMR using ^{1}H and ^{19}F nuclei (for $BMIm^+$ and $TFSI^-$ ions) and ^{7}Li or ^{133}Cs (for Li^+ and Cs^+ alkali cations). These elements are the only ones to present magnetic properties allowing to reach diffusion coefficients. For pure BMImTFSI, NMR and MD diffusion coefficients values are in good agreement. They show that $BMIm^+$ cation is slightly faster as $TFSI^-$ as expected from the ion mass differences and relatively well dissociated salt. The good agreement between MD and NMR measurements is also observed on a large temperature range (T = 300 K–353 K, Fig. 5c, Fig. S4a and Table S5). Both approaches show curved shapes which indicate that self-diffusion follows free volume like mechanisms (VTF model) as was already evidenced by ionic conductivity and viscosity measurements in our previous work[23] and for other ionic liquid-based electrolytes.[58,59]

Upon addition of alkali cation, the self diffusivities of BMIm and TFSI decrease while the added alkali get an even smaller diffusion coefficient – as was already measured in all alkali/ionic liquid mixtures.[37,43] Also, the self-diffusion coefficient of the added alkali/earth alkali cation is much slower than that of other cation and anion, even if its mass/ionic ratio is much smaller than other ions (with the exception of Cs^+ which is rather comparable). These trends and the D_i values measured from PFG-NMR measurements are in good agreement. This mobility decrease was also already measured in all kind of polymers and liquid electrolytes (including also many different ionic liquids), where Li^+ cations were always much slower than other ions.[60,61] This fact is related to the strong complexation of the alkali ion by few anions (3 or 4 generally, *cf.* structure analysis), therefore leading to much larger diffusing species or even larger aggregates containing few X^+ (see cluster analysis above). These effects are increasing for all ions when the amount of alkali salt f increases. For a given f ratio, the mobility decrease is more pronounced for the lighter alkali, Li^+ (lower polarizability/higher charge surface) and decreases as the alkali becomes bigger. The impact of adding the divalent earth alkaline Mg^{2+} is also more pronounced in the decrease of the diffusion coefficients. As these electrolytes have a potential application for next-generation electrolytes, it is helpful to determine the alkali transport number t_{alk} which is defined as:

$$t_{alk} = \frac{N_{alk} \times z_{alk} \times D_{alk}}{N_{alk} \times z_{alk} \times D_{alk} + N_{BMIm} \times z_{BMIm} \times D_{BMIm} + N_{TFSI} \times z_{TFSI} \times D_{TFSI}} \quad (4)$$

where N_{alk}, z_{alk}, N_{BMIm}, z_{BMIm}, N_{TFSI} and z_{TFSI} are respectively the molar fractions and the ionic charges for the alkali, BMIm and TFSI in the electrolytes. This dimensionless transport number is compared with those determined from NMR experiments in Table S5. This quantity is crucial in the frame of alkali transport efficiency. The reported values are very low (between 0.01 and 0.1), therefore reflecting the slow diffusion coefficients of

alkali compared to BMIm and TFSI. The values obtained from NMR self-diffusion coefficients (when available) are always larger than those obtained from MD. The values increase with the amount of added alkali, as the number of charge carrier increases. They are slightly higher for Cs^+ than Li^+, and much smaller in the case of the earth alkaline magnesium. All these arguments are also supported by the good agreement between experimental ionic conductivities and the Nernst–Einstein values computed from molecular dynamics (*cf.* Table S5). Ionic conductivities of Cs^+ based electrolytes are slightly larger than those based on Li^+, while those of based on Mg^{2+} are very low. A strong decrease of ionic conductivity is also measured upon increasing the concentration, as was already observed and discussed in previous studies.[37] The computed Nernst–Einstein values are around twice higher than those measured, which indicates a moderate dissociation ratio (~50%) in agreement with experimental measurements.[23]

4.3. Ion pairing and association

Peculiar properties of [X][BMImTFSI]*f* electrolytes are strongly related to the specific dynamics and availability of the X alkali/earth alkaline ions. These features can be depicted from the stability and lifetime of the complexation shell composed of $TFSI^-$ anions and the larger polyanionic clusters $X_n[(TFSI)_m]^{(m-n)-}$ in which at least two alkali cations are linked through anion bridges. If partial distribution functions $G_{AB}(r)$ and individual COM self-diffusion coefficients D_i give information about structure and dynamics averaged on the whole population of the simulation box, microscopic mechanisms involved in mobility processes may be gained from the analysis of ion cross-dynamics which measures the pairing time between two ions.[62] This is computed by the correlation function $P(t) = \langle\theta(t)\theta(0)\rangle$ where $\theta(t) = 1$ if both ions are adjacent at time t and $\theta(t) = 0$ otherwise.[63] The distance at which two ions are considered as adjacent corresponds to the first minimum in the $G_{A-B}(r)$ functions. These curves and the corresponding values are reported in Table S6. They spread in the range of 6 to 7 Å for X–TFSI pair and 9.5 to 10 Å for X–X and BMIm–TFSI pairs depending on the nature of the alkali. The pairing time distributions $P(t)$ for X–TFSI, X–X and BMIm–TFSI pairs determined at $T = 500$ K are presented in Fig. 6 for [X][BMImTFSI]f ($f = 0.2$ for Li and Cs, and $f = 0.1$ for Mg). These curves may be fitted by an exponential law $P(t) = P_0\exp(-t/\tau_c)$, and the characteristic relaxation decays τ_c are presented in the inset and in Table S7. The relaxation times corresponding to the solvent BMIm–TFSI are much shorter than those corresponding to the coordination of the cation X–TFSI and the longer one corresponds to the X–X proximity (*i.e.* the lifetime of the alkali based clusters). This could correspond to the fact that TFSI bonded to one Li cation is looser than those connected inside alkali multimers. All these pairs lifetimes are much longer for LiTFSI than CsTFSI based electrolytes and they slightly increase with the alkali concentration. This may be a molecular finding to explain the higher self-diffusion coefficients of Cs compared to Li at similar concentrations and temperatures (similar trends are also observed at $T = 300$ K as shown in Table S7).[64] In the case of

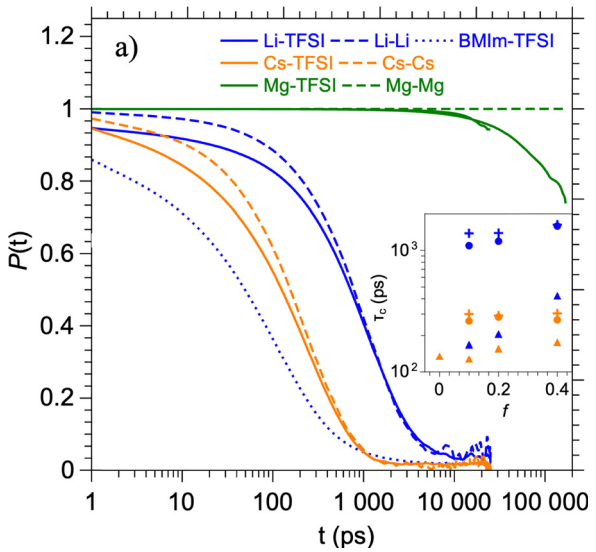

Fig. 6 Lifetime distribution of ion complexation and ion pairing/aggregation in [X][BMImTFSI]*f* electrolytes at $T = 500$ K. (a) Time correlation function $P(t)$ of ion/ion solvent [BMIm–TFSI], alkali coordination [X–TFSI] and aggregation [X–X] for X = Li, Cs and Mg. Ion pairing corresponds to distances between ions which are shorter than the first minimum of the $G(r)$ pair distributions. These distances are reported in Table S6. Inset: evolution of ion pairing time τ_c as a function of the ratio f at $T = 500$ K. The symbols correspond to the (●) X–TFSI (+) X–X and (▲) BMIm–TFSI ion pair correlations.

MgTFSI, the correlation time of BMIm–TFSI pair is rather comparable to those of alkali based systems (~200 ps) but the lifetime of the Mg^{2+} coordination shell is much longer than the calculated trajectory (~200 ns). This makes a major difference between earth alkaline and alkali cations. Upon decreasing the temperature to T 300 K, for [Li][BMImTFSI]*0.2* and [Cs][BMImTFSI]*0.2*, the lifetime of BMIm–TFSI correlation and those around the alkali increase considerably – it becomes larger than 12 ns (Table S7). Yet, it remains an order of magnitude below that for [Mg][BMImTFSI]0.1 at $T = 500$ K (even if the associated diffusion coefficients are much smaller). These differences may be related to our experimental studies which evidence slight differences between the nature of the dissolved cations and most specifically when comparing alkali to earth alkali.[23]

However, such a global/statistical MD analysis leads to the average behavior of the different species inside the [X][BMImTFSI]f electrolytes but lacks the molecular scale description of the molecular transport mechanisms. In fact, experiments describing these systems on large time/space scale evidence heterogeneous dynamics, with regions of slow and fast dynamics[65,66] which may be correlated to strong structural heterogeneities.[67] Recently, some refined approaches of self-diffusion coefficients as measured by PFG-NMR[66] or single-molecule tracking of probes[68] have shown multimodal dynamics – *i.e.* with mesoscopic domains having different mobilities correlated to the lifetime of structural correlations. In this context, more information on the heterogeneity in these electrolytes can be gained from the specific behavior of each

individual ion in using single-particle tracking strategy. As an example, individual MSDs for every ion of the [Li][BMImTFSI]*0.2* electrolyte at T = 300 K are presented in Fig. S9. This figure indicates that during the whole trajectory individual MSD spread over a large range of values for all ions. Even if very long trajectories are computed (~150 ns), individual MSD present meaningful evolution only up to 20 ns as statistics becomes poor over longer times. A more synthetic view of the spanning of these individual MSD inside this system is also presented in Fig. S10, which displays the evolution of all individual MSDs for the three families of ions: lithium, BMIm and TFSI. For each ion type, the two external bold lines represent the trajectories of the slowest and fastest ions while the dashed line represents the average behavior of each ion species (as discussed in previous sections). The pale tinted domains represent the scattering of the translational behavior of each species. Complementary information can be gained from the distribution of individual MSD at a fixed time P_{msd}, as represented with the histogram of Fig. 7a for a trajectory of 1 ns. At T = 300 K, a broad distribution of MSD is found for TFSI cations on the whole trajectory time – nearly spanning from those of Li^+ to those of the more rapid $BMIm^+$ cations. These data also indicate the scattering of the translations for Li^+ cations (*i.e.* the coexistence of slow and fast Li^+ over the whole trajectory), while all $BMIM^+$ cations behave nearly identically. Upon increasing the temperature to T = 500 K, the distribution of MSD is narrow for the three cation types and no overlap of the MSD is found on the whole trajectory.

Identically, Fig. 7b presents the individual MSD behavior for [Mg][BMImTFSI]*0.1* electrolyte at T = 500 K. While the averaged MSD of the three species are rather similar to those in [Li][BMImTFSI]*0.2* at the same temperatures (see also Table S5), MSD of TFSI present a strictly bimodal distribution: MSDs of the slowest $TFSI^-$ being similar to thus of the Mg^{2+} ions, while the fastest $TFSI^-$ anions corresponds to those of the $BMIm^+$ cations. These observations strongly suggest that [Mg][BMImTFSI]*0.1* behaves as a dynamical biphasic system in which cation–anion pairing (both for Mg–TFSI and BMIm–TFSI) remains on a very long time scale and even for duration long enough to reach the Fick self-diffusion regime. This is in complete agreement with the lifetime of ion complexation and ion pairing/aggregation time constant as detailed above (Fig. 6 and Table S7). It may also explain experimental findings such as the change in the Walden exponent.[2,3]

As a further step, we delve the coupling between individual dynamics and the corresponding local structure (ion pairing, ion aggregates, *etc*...) along the trajectory of specific ions – *i.e.* those that can be considered as 'slow', 'fast' or 'mean' depending where they stand in the MSD distributions. This is illustrated in Fig. 8, which presents the time evolution of the TFSI–Li pair distribution function along a trajectory for a selected 'mean' TFSI. This one was intentionally chosen as showcase. However, additional data obtained with various Li and TFSI ions in the same mixture support the same conclusions (Fig. S11). In this Figure, the time evolution of the pair distribution function $G_{TFSI-Li}(r,t) = f(t)$ is sketched using 2D level maps and subsequent projections are added to gain further insights. Upper traces correspond to horizontal projections of the $G(r) = f(t)$ 2D maps at specific times to highlight the evolution of pair distribution functions $G_{TFSI-Li}(r)$, $G_{TFSI-BMIm}(r)$ and $G_{TFSI-TFSI}(r)$. The curve on the left side represents the evolution of the "instantaneous individual MSD" of this ion as calculated for a duration of 2 ns along the trajectory ($MSD_{2\,ns}$). The 2D projection map clearly indicates major temporal variations of $G_{TFSI-Li}(r)$ around the selected TFSI anion. This evolution is also supported by the selected $G_{AB}(r)$ presented as the top projection. Successively, this TFSI is not coordinated by Li^+ cations (0–25 ns), then coordinated to one Li^+ cation (25–145 ns) and then by to two Li^+ cations after 145 ns. The second coordination shell corresponding to farther TFSI–BMIm and TFSI–TFSI correlations are rather constant during the whole trajectory.

Changes between these different coordination schemes influence concomitantly the dynamics as evidenced by the measurement of $MSD_{2\,ns}$, which strongly decreases as the local

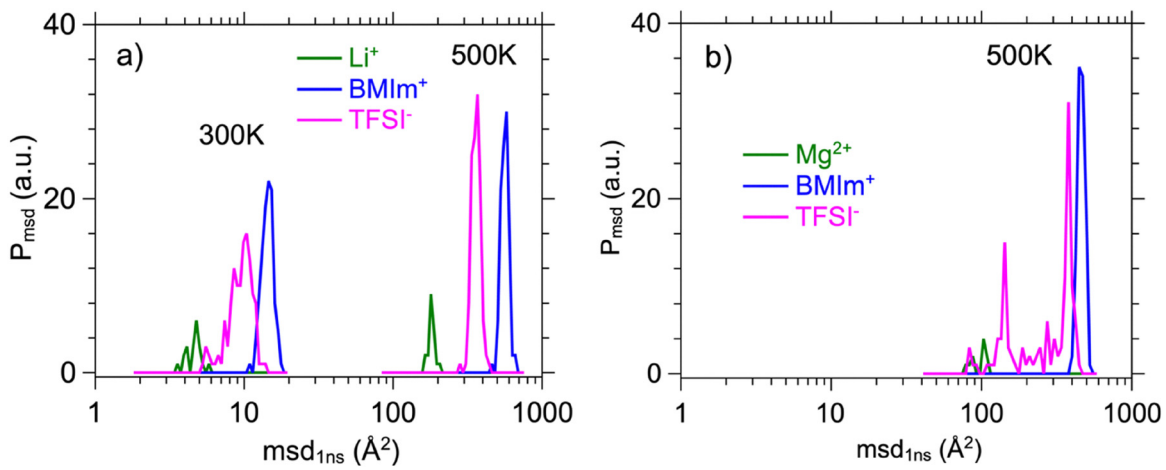

Fig. 7 Distribution of MSD (P_{msd}) as measured for a trajectory of 1 ns for the three species inside: (a) X = Li, f = 0.2, T = 300 K and T = 500 K and (b) X = Mg, f = 0.1, T = 500 K.

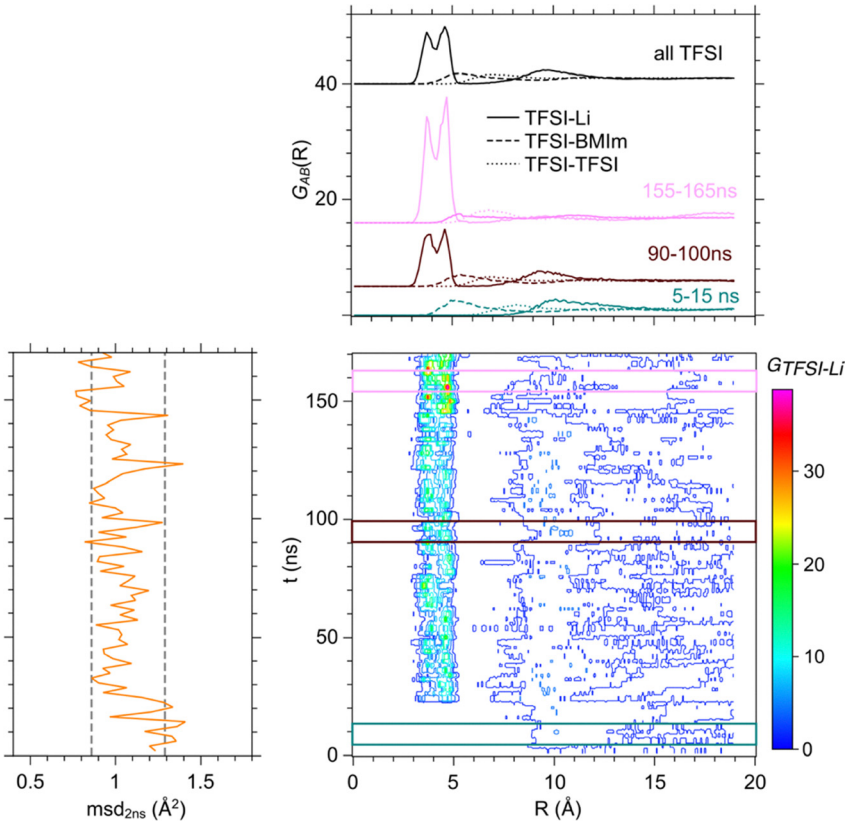

Fig. 8 Time dependence of the radial distribution function for a selected 'mean' TFSI in [Li][BMIm][TFSI]*0.2* at T = 300 K. A sampling of 2 ns was selected to obtain statistically relevant dynamical, structural and cross-coupled information. Central view: 2D level map for $G_{TFSI-Li}(r)$. Top: projections of $G_{AB}(r)$ for selected trajectory sections as underlined by the color rectangle on 2D map. Left: MSD calculated for a 2 ns range ($MSD_{2\,ns}$) along the trajectory. $msd_{2\,ns}$ corresponding to "slow" and "fast" regime also presented as dashed lines.

coordination shell becomes bigger and consists of more Li neighbors around TFSI. These conclusions are corroborated by monitoring the behavior of fast and slow TFSI (Fig. 9a and b), which present respectively no and two Li^+ cations in the coordination shell of $TFSI^-$ during the whole trajectory. This indicates the strong coupling between local structural and dynamical heterogeneities. Li^+ cations have similar heterogeneous behavior (Fig. S11a–c) but coordination shells are more complex and could involve temporarily some various geometries corresponding to $Li^+\cdots Li^+$ clusters engaging different TFSI bridging geometries, as explained in a previous section. Similar phenomena are also observed for [Mg][BMImTFSI] (Fig. S12), therefore further indicating the strong synergy between ion coordination spheres and their dynamics. This also indicates that during the whole trajectory and even at T = 500 K, Mg^{2+} ions are either only complexed by TFSI anions or making stable ion clusters.

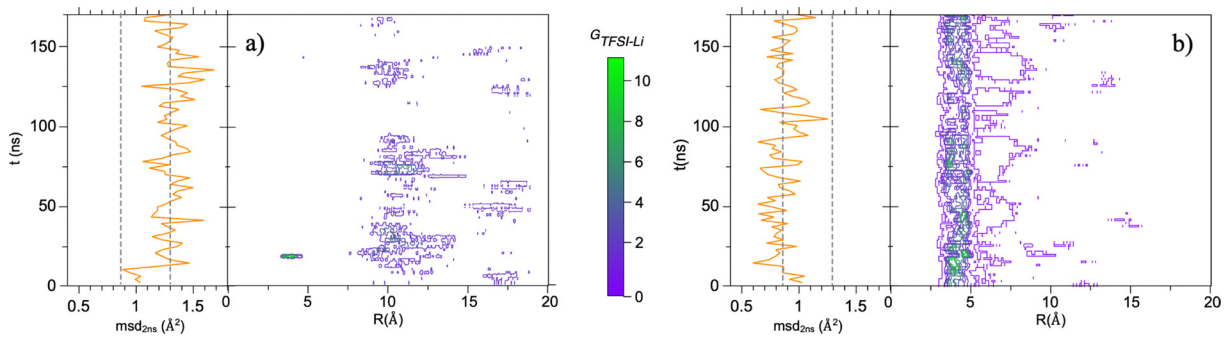

Fig. 9 Time dependence of the radial distribution function along a 170 ns trajectory for [Li][BMIm][TFSI]*0.2* at 300 K around selected individual anions: (a) fast and (b) slow $TFSI^-$. A sampling of 2 ns was selected to obtain clear-cut dynamical, structural and cross-coupled informations. Central: 2D level map for $G_{TFSI-Li}$. Left: msd calculated for 2 ns range ($msd_{2\,ns}$) along the trajectory. $msd_{2\,ns}$ correspondinng to "slow" and "fast" regime also presented as pale colored broad vertical lines.

5. Conclusion

This study investigated the use of ionic liquids (ILs) as versatile solvents for alkali and alkaline earth salts, highlighting their potential as promising electrolytes for Li and post-Li batteries. By focusing on the iconic IL 1-butyl-3-methylimidazolium trifluoromethylsulfonimide (BMImTFSI) with dissolved alkali (Li^+, Na^+, K^+, Cs^+) and alkaline earth (Mg^{2+}) TFSI salts, we demonstrated how classical molecular dynamics (MD) simulations can effectively reproduce structural and dynamical effects in these complex liquids, *i.e.* the local nanoorganization and the self-diffusion coefficients as measured through wide-angle X-ray scattering and pulsed-field gradient NMR measurements respectively on a large range of temperatures. The choice of a small system size,[34] and of classical force field allows us to reproduce all the dynamical trends of electrolytes with a consequent gain of computing times compared to those involved with polarizable force field.[69,70] The diffusion coefficient values are still lower, and scaled forcefield with reduced partial charge, *i.e.* $q = \pm 0.7$ is sometimes used to compensate rather arbitrarily these effects.[71] However larger simulation boxes are needed to avoid finite size artefacts in the structural properties. All these protocols allow us to reveal the subtle behavior differences between electrolytes containing alkali and alkaline earth ions, which appear to be strongly connected to the lifetime association of the cation and TFSI anions. One step ahead of standard statistical analysis of experimental results or MD trajectories, single-particle tracking strategies reveal uncovered correlations between structural and dynamical heterogeneities across multiple scales – from coordination spheres to nanosegregation and from picoseconds to hundreds of nanoseconds time scales. This work not only advances our understanding of IL-based electrolytes but also paves the way for the development of more efficient and stable energy storage solutions.

Author contributions

Patrick Judeinstein: writing – review & editing, writing – original draft, visualization, validation, supervision, resources, methodology, investigation, funding acquisition, formal analysis, data curation, conceptualization, software. Hoang Phuong Khanh Ngo: visualization, investigation, resources. Fabrice Cousin: writing – review & editing, visualization, methodology, investigation, formal analysis. Cristina Iojoiu: writing – review & editing, supervision, funding acquisition, project administration, investigation. Emilie Planes: writing – review & editing, supervision, investigation. Benoît Coasne: writing – review & editing, writing – original draft, visualization, validation, methodology, investigation, funding acquisition, formal analysis, data curation, conceptualization, software.

Conflicts of interest

There are no conflicts to declare.

Data availability

All data are included within this submission.

Supplementary information: additional details on molecular dynamics methodology and results, additional WAXS, PFG-NMR and ionic conductivity results. See DOI: https://doi.org/10.1039/d5cp04760a.

Acknowledgements

The authors acknowledge the Centre Informatique National de l'Enseignement Supérieur (CINES) for a generous allocation of computing time (project: A0040807695) and the Dahu platform of the GRICAD infrastructure (https://gricad.univ-grenoble-alpes.fr), which is supported by the Rhone-Alpes region (GRANT CPER07-13 CIRA) and the Equip@Meso project (ANR-10-EQPX-29-01) of the programme Investissements d'Avenir supervised by the French Research Agency. We acknowledge the Minister for Higher Education and Scientific Research for PhD grant of Khanh Ngo and CNRS and CEA for their recurrent funding for research.

References

1 Y. Marcus, *Ionic Liquid Properties From Molten Salts to RTILs*, Springer, Cham, 2016.
2 R. Shi and Y. Wang, Dual Ionic and Organic Nature of Ionic Liquids, *Sci. Rep.*, 2016, **6**(1), 19644, DOI: 10.1038/srep19644.
3 R. Hayes, G. G. Warr and R. Atkin, Structure and Nanostructure in Ionic Liquids, *Chem. Rev.*, 2015, **115**(13), 6357–6426, DOI: 10.1021/cr500411q.
4 F. Ferdeghini, Q. Berrod, J.-M. Zanotti, P. Judeinstein, V. G. Sakai, O. Czakkel, P. Fouquet and D. Constantin, Nanostructuration of Ionic Liquids: Impact on the Cation Mobility. A Multi-Scale Study, *Nanoscale*, 2017, **9**(5), 1901–1908, DOI: 10.1039/C6NR07604A.
5 Y.-L. Wang, B. Li, S. Sarman, F. Mocci, Z.-Y. Lu, J. Yuan, A. Laaksonen and M. D. Fayer, Microstructural and Dynamical Heterogeneities in Ionic Liquids, *Chem. Rev.*, 2020, **120**(13), 5798–5877, DOI: 10.1021/acs.chemrev.9b00693.
6 R. Giernoth, Task-Specific Ionic Liquids, *Angew. Chem., Int. Ed.*, 2010, **49**(16), 2834–2839, DOI: 10.1002/anie.200905981.
7 H. Olivier-Bourbigou, L. Magna and D. Morvan, Ionic Liquids and Catalysis: Recent Progress from Knowledge to Applications, *Appl. Catal., A*, 2010, **373**(1–2), 1–56, DOI: 10.1016/j.apcata.2009.10.008.
8 D. R. MacFarlane; J. M. Pringle and M. Kar, *Fundamentals of Ionic Liquids*, Wiley-VCH, Weinheim, Germany, 2017, DOI: 10.1002/9783527340033.
9 G. Kaur, H. Kumar and M. Singla, Diverse Applications of Ionic Liquids: A Comprehensive Review, *J. Mol. Liq.*, 2022, **351**, 118556, DOI: 10.1016/j.molliq.2022.118556.
10 M. Watanabe, M. L. Thomas, S. Zhang, K. Ueno, T. Yasuda and K. Dokko, Application of Ionic Liquids to Energy

Storage and Conversion Materials and Devices, *Chem. Rev.*, 2017, **117**(10), 7190–7239, DOI: 10.1021/acs.chemrev.6b00504.

11 M. Armand, F. Endres, D. R. MacFarlane, H. Ohno and B. Scrosati, Ionic-Liquid Materials for the Electrochemical Challenges of the Future, *Nat. Mater.*, 2009, **8**(8), 621–629, DOI: 10.1038/nmat2448.

12 K. Matuszek, S. L. Piper, A. Brzęczek-Szafran, B. Roy, S. Saher, J. M. Pringle and D. R. MacFarlane, Unexpected Energy Applications of Ionic Liquids, *Adv. Mater.*, 2024, **36**(23), 2313023, DOI: 10.1002/adma.202313023.

13 O. Borodin, G. A. Giffin, A. Moretti, J. B. Haskins, J. W. Lawson, W. A. Henderson and S. Passerini, Insights into the Structure and Transport of the Lithium, Sodium, Magnesium, and Zinc Bis(Trifluoromethansulfonyl)Imide Salts in Ionic Liquids, *J. Phys. Chem. C*, 2018, **122**(35), 20108–20121, DOI: 10.1021/acs.jpcc.8b05573.

14 K. Matsumoto, J. Hwang, S. Kaushik, C.-Y. Chen and R. Hagiwara, Advances in Sodium Secondary Batteries Utilizing Ionic Liquid Electrolytes, *Energy Environ. Sci.*, 2019, **12**(11), 3247–3287, DOI: 10.1039/C9EE02041A.

15 T. Yamamoto, K. Matsumoto, R. Hagiwara and T. Nohira, Physicochemical and Electrochemical Properties of $K[N(SO_2F)_2]$–[N-Methyl-N-Propylpyrrolidinium][$N(SO_2F)_2$] Ionic Liquids for Potassium-Ion Batteries, *J. Phys. Chem. C*, 2017, **121**(34), 18450–18458, DOI: 10.1021/acs.jpcc.7b06523.

16 T. Kakibe, N. Yoshimoto, M. Egashira and M. Morita, Optimization of Cation Structure of Imidazolium-Based Ionic Liquids as Ionic Solvents for Rechargeable Magnesium Batteries, *Electrochem. Commun.*, 2010, **12**(11), 1630–1633, DOI: 10.1016/j.elecom.2010.09.012.

17 M. L. Dietz, Ionic Liquids as Extraction Solvents: Where Do We Stand?, *Sep. Sci. Technol.*, 2006, **41**(10), 2047–2063, DOI: 10.1080/01496390600743144.

18 R. G. Pearson, Hard and Soft Acids and Bases, *J. Am. Chem. Soc.*, 1963, **85**(22), 3533–3539, DOI: 10.1021/ja00905a001.

19 A. B. Pereiro, J. M. M. Araújo, F. S. Oliveira, J. M. S. S. Esperança, J. N. Canongia Lopes, I. M. Marrucho and L. P. N. Rebelo, Solubility of Inorganic Salts in Pure Ionic Liquids, *J. Chem. Thermodyn.*, 2012, **55**, 29–36, DOI: 10.1016/j.jct.2012.06.007.

20 J. M. Vicent-Luna, E. Azaceta, S. Hamad, J. M. OrtiRoldán, R. Tena-Zaera, S. Calero and J. A. Anta, Molecular Dynamics Analysis of Charge Transport in Ionic-Liquid Electrolytes Containing Added Salt with Mono, Di, and Trivalent Metal Cations, *ChemPhysChem*, 2018, **19**(13), 1665–1673, DOI: 10.1002/cphc.201701326.

21 S. Kunigal Vijaya Shankar, Y. Claveau, T. Rasoanarivo, C. Ewels and J. Le Bideau, Impact of Li, Na and Zn Metal Cation Concentration in EMIM–TFSI Ionic Liquids on Ion Clustering, Structure and Dynamics, *Phys. Chem. Chem. Phys.*, 2024, **26**(8), 7049–7059, DOI: 10.1039/D3CP06315A.

22 C. J. Clarke, T. Clayton, M. J. Palmer, K. R. J. Lovelock and P. Licence, A Thermophysical Investigation of Weakly Coordinated Metals in Ionic Liquids, *Chem. Sci.*, 2024, **15**(34), 13832–13840, DOI: 10.1039/D4SC03588G.

23 H. P. K. Ngo, E. Planes, C. Iojoiu, P. Soudant, A.-L. Rollet and P. Judeinstein, Transport Properties of Alkali/Alkaline Earth Cations in Ionic-Liquid Based Electrolytes, *J. Ion. Liq.*, 2022, **2**(2), 100044, DOI: 10.1016/j.jil.2022.100044.

24 M. McLin and C. A. Angell, Contrasting Conductance/Viscosity Relations in Liquid States of Vitreous and Polymer Solid Electrolytes, *J. Phys. Chem.*, 1988, **92**(8), 2083–2086, DOI: 10.1021/j100319a002.

25 F. Lo Celso, G. B. Appetecchi, E. Simonetti, M. Zhao, E. W. Castner, U. Keiderling, L. Gontrani, A. Triolo and O. Russina, Microscopic Structural and Dynamic Features in Triphilic Room Temperature Ionic Liquids, *Front. Chem.*, 2019, **7**, 285, DOI: 10.3389/fchem.2019.00285.

26 Y. Umebayashi, T. Mitsugi, S. Fukuda, T. Fujimori, K. Fujii, R. Kanzaki, M. Takeuchi and S.-I. Ishiguro, Lithium Ion Solvation in Room-Temperature Ionic Liquids Involving Bis(Trifluoromethanesulfonyl) Imide Anion Studied by Raman Spectroscopy and DFT Calculations, *J. Phys. Chem. B*, 2007, **111**(45), 13028–13032, DOI: 10.1021/jp076869m.

27 E. O. Stejskal and J. E. Tanner, Spin Diffusion Measurements: Spin Echoes in the Presence of a Time-Dependent Field Gradient, *J. Chem. Phys.*, 1965, **42**(1), 288–292, DOI: 10.1063/1.1695690.

28 A. P. Thompson, H. M. Aktulga, R. Berger, D. S. Bolintineanu, W. M. Brown, P. S. Crozier, P. J. in 't Veld, A. Kohlmeyer, S. G. Moore, T. D. Nguyen, R. Shan, M. J. Stevens, J. Tranchida, C. Trott and S. J. Plimpton, LAMMPS - a Flexible Simulation Tool for Particle-Based Materials Modeling at the Atomic, Meso, and Continuum Scales, *Comput. Phys. Commun.*, 2022, **271**, 108171, DOI: 10.1016/j.cpc.2021.108171.

29 J. N. Canongia Lopes, J. Deschamps and A. A. H. Pádua, Modeling Ionic Liquids Using a Systematic All-Atom Force Field, *J. Phys. Chem. B*, 2004, **108**(6), 2038–2047, DOI: 10.1021/jp0362133.

30 T. Köddermann, D. Paschek and R. Ludwig, Molecular Dynamic Simulations of Ionic Liquids: A Reliable Description of Structure, Thermodynamics and Dynamics, *ChemPhysChem*, 2007, **8**(17), 2464–2470, DOI: 10.1002/cphc.200700552.

31 D. Horinek, S. I. Mamatkulov and R. R. Netz, Rational Design of Ion Force Fields Based on Thermodynamic Solvation Properties, *J. Chem. Phys.*, 2009, **130**(12), 124507, DOI: 10.1063/1.3081142.

32 S. Mamatkulov, M. Fyta and R. R. Netz, Force Fields for Divalent Cations Based on Single-Ion and Ion-Pair Properties, *J. Chem. Phys.*, 2013, **138**(2), 024505, DOI: 10.1063/1.4772808.

33 B. Coasne, L. Viau and A. Vioux, Loading-Controlled Stiffening in Nanoconfined Ionic Liquids, *J. Phys. Chem. Lett.*, 2011, **2**(10), 1150–1154, DOI: 10.1021/jz200411a.

34 S. Gabl, C. Schröder and O. Steinhauser, Computational Studies of Ionic Liquids: Size Does Matter and Time Too, *J. Phys. Chem. Lett.*, 2012, **137**(9), 094501, DOI: 10.1063/1.4748352.

35 S. Nosé, A Unified Formulation of the Constant Temperature Molecular Dynamics Methods, *J. Chem. Phys.*, 1984, **81**(1), 511–519, DOI: 10.1063/1.447334.

36 A. Martinelli, M. Maréchal, Å. Östlund and J. Cambedouzou, Insights into the Interplay between Molecular Structure and Diffusional Motion in 1-Alkyl-3-Methylimidazolium Ionic Liquids: A Combined PFG NMR and X-Ray Scattering Study, *Phys. Chem. Chem. Phys.*, 2013, **15**(15), 5510, DOI: 10.1039/c3cp00097d.

37 P. Judeinstein, M. Zeghal, D. Constantin, C. Iojoiu and B. Coasne, Interplay of Structure and Dynamics in Lithium/Ionic Liquid Electrolytes: Experiment and Molecular Simulation, *J. Phys. Chem. B*, 2021, **125**(6), 1618–1631, DOI: 10.1021/acs.jpcb.0c09597.

38 L. Aguilera, J. Völkner, A. Labrador and A. Matic, The Effect of Lithium Salt Doping on the Nanostructure of Ionic Liquids, *Phys. Chem. Chem. Phys.*, 2015, **17**(40), 27082–27087, DOI: 10.1039/C5CP03825A.

39 A. Triolo, O. Russina, H.-J. Bleif and E. Di Cola, Nanoscale Segregation in Room Temperature Ionic Liquids, *J. Phys. Chem. B*, 2007, **111**(18), 4641–4644, DOI: 10.1021/jp067705t.

40 N. C. Boaz, E. L. Smigla, C. Stippich, C. Voss and N. A. Mauro, X-Ray Scattering Investigation of Ion Aggregation in Imidazolium-Based Ionic Liquids upon Doping with Lithium, Sodium, Potassium, Rubidium and Cesium Salts, *J. Mol. Liq.*, 2020, **302**, 112540, DOI: 10.1016/j.molliq.2020.112540.

41 A. Ordikhani Seyedlar, S. Stapf and C. Mattea, Dynamics of the Ionic Liquid 1-Butyl-3-Methylimidazolium Bis(Trifluoromethylsulphonyl)Imide Studied by Nuclear Magnetic Resonance Dispersion and Diffusion, *Phys. Chem. Chem. Phys.*, 2015, **17**(3), 1653–1659, DOI: 10.1039/C4CP04178J.

42 M. Y. Yang, B. V. Merinov, S. V. Zybin, W. A. Goddard, E. K. Mok, H. J. Hah, H. E. Han, Y. C. Choi and S. H. Kim, Transport Properties of Imidazolium Based Ionic Liquid Electrolytes from Molecular Dynamics Simulations, *Electrochem. Sci. Adv.*, 2022, **2**(2), e2100007, DOI: 10.1002/elsa.202100007.

43 M. L. P. Le, F. Alloin, P. Strobel, J.-C. Leprêtre, C. Pérez Del Valle and P. Judeinstein, Structure−Properties Relationships of Lithium Electrolytes Based on Ionic Liquid, *J. Phys. Chem. B*, 2010, **114**(2), 894–903, DOI: 10.1021/jp9098842.

44 O. Karé, A. De Souza Braga Neto, B. Rigaud, Q. Berrod, S. Lyonnard, C. Cousin, J. Sirieix-Plénet, A.-L. Rollet and G. Mériguet, NMR Investigation of Multi-Scale Dynamics in Ionic Liquids Containing Li+ and La3 +: From Vehicular to Hopping Transport Mechanism, *J. Ion. Liq.*, 2024, **4**(1), 100087, DOI: 10.1016/j.jil.2024.100087.

45 I. Nicotera, C. Oliviero, W. A. Henderson, G. B. Appetecchi and S. Passerini, NMR Investigation of Ionic Liquid−LiX Mixtures: Pyrrolidinium Cations and TFSI- Anions, *J. Phys. Chem. B*, 2005, **109**(48), 22814–22819, DOI: 10.1021/jp053799f.

46 F. Chen and M. Forsyth, Elucidation of Transport Mechanism and Enhanced Alkali Ion Transference Numbers in Mixed Alkali Metal–Organic Ionic Molten Salts, *Phys. Chem. Chem. Phys.*, 2016, **18**(28), 19336–19344, DOI: 10.1039/C6CP01411A.

47 A. Andriola, K. Singh, J. Lewis and L. Yu, Conductivity, Viscosity, and Dissolution Enthalpy of LiNTF2 in Ionic Liquid $BMINTF_2$, *J. Phys. Chem. B*, 2010, **114**(36), 11709–11714, DOI: 10.1021/jp1044404.

48 Z. Li, G. D. Smith and D. Bedrov, Li^+ Solvation and Transport Properties in Ionic Liquid/Lithium Salt Mixtures: A Molecular Dynamics Simulation Study, *J. Phys. Chem. B*, 2012, **116**(42), 12801–12809, DOI: 10.1021/jp3052246.

49 Y. Marcus, Effect of Ions on the Structure of Water: Structure Making and Breaking, *Chem. Rev.*, 2009, **109**(3), 1346–1370, DOI: 10.1021/cr8003828.

50 D. A. Keen, A Comparison of Various Commonly Used Correlation Functions for Describing Total Scattering, *J. Appl. Crystallogr.*, 2001, **34**(2), 172–177, DOI: 10.1107/S0021889800019993.

51 N. W. Ashcroft and D. C. Langreth, Structure of Binary Liquid Mixtures. I, *Phys. Rev.*, 1967, **156**(3), 685–692, DOI: 10.1103/PhysRev.156.685.

52 J. C. Araque, J. J. Hettige and C. J. Margulis, Modern Room Temperature Ionic Liquids, a Simple Guide to Understanding Their Structure and How It May Relate to Dynamics, *J. Phys. Chem. B*, 2015, **119**(40), 12727–12740, DOI: 10.1021/acs.jpcb.5b05506.

53 J.-C. Lassègues, J. Grondin, C. Aupetit and P. Johansson, Spectroscopic Identification of the Lithium Ion Transporting Species in LiTFSI-Doped Ionic Liquids, *J. Phys. Chem. A*, 2009, **113**(1), 305–314, DOI: 10.1021/jp806124w.

54 M. Casalegno, G. Raos, G. B. Appetecchi, S. Passerini, F. Castiglione and A. Mele, From Nanoscale to Microscale: Crossover in the Diffusion Dynamics within Two Pyrrolidinium-Based Ionic Liquids, *J. Phys. Chem. Lett.*, 2017, **8**(20), 5196–5202, DOI: 10.1021/acs.jpclett.7b02431.

55 D. A. Schmidt, Ö. Birer, S. Funkner, B. P. Born, R. Gnanasekaran, G. W. Schwaab, D. M. Leitner and M. Havenith, Rattling in the Cage: Ions as Probes of Sub-Picosecond Water Network Dynamics, *J. Am. Chem. Soc.*, 2009, **131**(51), 18512–18517, DOI: 10.1021/ja9083545.

56 O. O. Postupna, Y. V. Kolesnik, O. N. Kalugin and O. V. Prezhdo, Microscopic Structure and Dynamics of $LiBF_4$ Solutions in Cyclic and Linear Carbonates, *J. Phys. Chem. B*, 2011, **115**(49), 14563–14571, DOI: 10.1021/jp206006m.

57 D. Sharma and A. Chandra, Terahertz Spectroscopy of Aqueous Solutions of Alkali (M) Chlorides Using Polarizable Models: Self- and Cross-Correlation Contributions of Ions and Hydration Shell Water for M^+ = Li^+, Na^+, K^+, Rb^+, and Cs, *J. Phys. Chem. B*, 2025, **129**(24), 6050–6060, DOI: 10.1021/acs.jpcb.5c01907.

58 M. Nahra, E. Chainet, L. Svecova, L. Cointeaux and I. Billard, Reliability of Arrhenius and Several VTF Laws to Describe the Effect of TaF5 Addition onto the Transport Properties of 1-Butyl-1-Methylpyrrolidinium Bis(Trifluoromethylsulfonyl)Imide, *Fluid Phase Equilib.*, 2016, **415**, 101–109, DOI: 10.1016/j.fluid.2016.01.043.

59 V. Chaudoy, J. Jacquemin, F. Tran-Van, M. Deschamps and F. Ghamouss, Effect of Mixed Anions on the Transport Properties and Performance of an Ionic Liquid-Based Electrolyte for Lithium-Ion Batteries, *Pure Appl. Chem.*, 2019, **91**(8), 1361–1381, DOI: 10.1515/pac-2018-1006.

60 K. Hayamizu, Y. Aihara, S. Arai and W. S. Price, Self-Diffusion Coefficients of Lithium, Anion, Polymer, and Solvent in Polymer Gel Electrolytes Measured Using ^{7}Li, ^{19}F, and ^{1}H Pulsed-Gradient Spin-Echo NMR, *Electrochim. Acta*, 2000, **45**(8–9), 1313–1319, DOI: 10.1016/S0013-4686(99)00338-2.

61 P. M. Richardson, A. M. Voice and I. M. Ward, Pulsed-Field Gradient NMR Self Diffusion and Ionic Conductivity Measurements for Liquid Electrolytes Containing $LiBF_4$ and Propylene Carbonate, *Electrochim. Acta*, 2014, **130**, 606–618, DOI: 10.1016/j.electacta.2014.03.072.

62 W. Zhao, F. Leroy, B. Heggen, S. Zahn, B. Kirchner, S. Balasubramanian and F. Müller-Plathe, Are There Stable Ion-Pairs in Room-Temperature Ionic Liquids? Molecular Dynamics Simulations of 1-*n*-Butyl-3-Methylimidazolium Hexafluorophosphate, *J. Am. Chem. Soc.*, 2009, **131**(43), 15825–15833, DOI: 10.1021/ja906337p.

63 P.-A. Cazade, R. Hartkamp and B. Coasne, Structure and Dynamics of an Electrolyte Confined in Charged Nanopores, *J. Phys. Chem. C*, 2014, **118**(10), 5061–5072, DOI: 10.1021/jp4098638.

64 Y. Zhang and E. J. Maginn, Direct Correlation between Ionic Liquid Transport Properties and Ion Pair Lifetimes: A Molecular Dynamics Study, *J. Phys. Chem. Lett.*, 2015, **6**(4), 700–705, DOI: 10.1021/acs.jpclett.5b00003.

65 Q. Berrod, F. Ferdeghini, J.-M. Zanotti, P. Judeinstein, D. Lairez, V. García Sakai, O. Czakkel, P. Fouquet and D. Constantin, Ionic Liquids: Evidence of the Viscosity Scale-Dependence, *Sci. Rep.*, 2017, **7**(1), 2241, DOI: 10.1038/s41598-017-02396-7.

66 S. Miao, A. Sardharwalla and S. Perkin, Ion Diffusion Reveals Heterogeneous Viscosity in Nanostructured Ionic Liquids, *J. Phys. Chem. Lett.*, 2024, **15**(47), 11855–11861, DOI: 10.1021/acs.jpclett.4c02996.

67 R. Ogbodo, W. V. Karunaratne, G. R. Acharya, M. S. Emerson, M. Mughal, H. M. Yuen, N. Zmich, S. Nembhard, F. Wang, H. Shirota, S. I. Lall-Ramnarine, E. W. Castner, J. F. Wishart, A. J. Nieuwkoop and C. J. Margulis, Structural Origins of Viscosity in Imidazolium and Pyrrolidinium Ionic Liquids Coupled with the NTf_2^- Anion, *J. Phys. Chem. B*, 2023, **127**(28), 6342–6353, DOI: 10.1021/acs.jpcb.3c02604.

68 J. Opare-Addo, I. Morgan, N. Tryon-Tasson, D. F. Twedt-Gutierrez, J. L. Anderson, J. W. Petrich, X. Song and E. A. Smith, Nanodomains and Their Temperature Dependence in a Phosphonium-Based Ionic Liquid: A Single-Molecule Tracking Study, *J. Phys. Chem. B*, 2024, **128**(47), 11714–11722, DOI: 10.1021/acs.jpcb.4c05184.

69 P.-A. Cazade, J. Dweik, B. Coasne, F. Henn and J. Palmeri, Molecular Simulation of Ion-Specific Effects in Confined Electrolyte Solutions Using Polarizable Forcefields, *J. Phys. Chem. C*, 2010, **114**(28), 12245–12257, DOI: 10.1021/jp103880s.

70 D. Bedrov, J.-P. Piquemal, O. Borodin, A. D. MacKerell, B. Roux and C. Schröder, Molecular Dynamics Simulations of Ionic Liquids and Electrolytes Using Polarizable Force Fields, *Chem. Rev.*, 2019, **119**(13), 7940–7995, DOI: 10.1021/acs.chemrev.8b00763.

71 C. Schröder, Comparing Reduced Partial Charge Models with Polarizable Simulations of Ionic Liquids, *Phys. Chem. Chem. Phys.*, 2012, **14**(9), 3089–3102, DOI: 10.1039/C2CP23329K.